 MCB, vol.8, no.1, pp.21-42, 2011

Comparison of Hemodynamic Endpoints between Normal Subject and Tetralogy Patient Using Womersley Velocity Profile and MR Based Flow Measurements

Ashish Das[*], **William M. Gottliebson**[†,‡], **Madhura Karve**[*]
Rupak Banerjee[*,§,¶]

Abstract: Right ventricular (RV) enlargement and pulmonary valve insufficiency (PI) are well-known, unavoidable long term sequelae encountered by patients who undergo tetralogy of Fallot (TOF) surgery. Despite their lifelong need for cardiac surveillance and occasional re-intervention, there is a paucity of numerical data characterizing blood flows in their pulmonary arteries (PA). Specifically, although PA regurgitation is well-known to be ubiquitously present in adult repaired TOF (rTOF) patients yet, there have been only limited numerical studies to fully characterize this process. The few studies available have utilized idealized, simplistic geometric models or overly simplistic boundary conditions that fail to account for flow reversals near the arterial walls as observed in *in-vitro* and MRI based *in-vivo* studies. The objective of this study was to establish and validate a numerical methodology of PA blood flow using actual patient specific geometry and flow measurements obtained using phase-contrast MRI, employing Womersley type velocity profiles that model flow reversals near walls.

The results from computation were validated with measurements. For the normal subject, the time averaged right PA pressure from computation (13.8 mmHg) and experiment (14.6 mmHg) differed by 6%. The time-averaged main PA pressure from computation (16.5 mmHg) and experiment (16.3 mmHg) differed by 1%. The numerically computed left PA regurgitant fraction was 89% compared to measured 77.5%, while the same for the rTOF was 43% (computation), compared to 39.6% (measured). We conclude that the use of numerical computations using the Womersley boundary condition allows reliable modeling of the pathophysiology of PA

[*] School of Dynamic System, University of Cincinnati, Cincinnati, Ohio.
[†] Heart Institute, Division of Pediatric Cardiology, Cincinnati Children's Hospital and Medical Center, Cincinnati, Ohio.
[‡] College of Medicine, University of Cincinnati, Cincinnati, Ohio.
[§] Department of Biomedical Engineering, University of Cincinnati, Cincinnati, Ohio.
[¶] Corresponding author: Tel: (513) 556 2124; fax: (513) 556 3390. e-mail: Rupak.Banerjee@uc.edu

flow in rTOF.

Keywords: Tetralogy of fallot, pulmonary insufficiency, cine-phase contrast velocity, Pulmonary regurgitation.

1 Introduction

Tetralogy of Fallot (TOF), the most common cause of "blue-baby syndrome" consists of four interrelated anatomical defects: 1) *Ventricular Septal Defect*: a hole between the right and the left ventricle, 2) *Pulmonary Stenois*: constriction of the pulmonary outflow tract, 3) *RV Hypertrophy*: pressure overloading of RV, and 4) *Overriding Aorta*: Aorta overrides the RV. TOF has now been successfully repaired in infants and small children for more than 50 years. Consequently, there are now an estimated 100,000 adult "repaired TOF" (rTOF) patients in the United States alone, and thus, the long-term sequelae of the disease, namely PI and RV enlargement, have become important. The pathophysiology of rTOF with pulmonary valve insufficiency (PI) is well documented [d'Udekem et al., 2000; Park 1996] and consists of alteration in diastolic right ventricular (RV) loading conditions, triggering RV hypertrophy and dilatation. In turn, RV dilatation can evolve into irreversible RV myocardial contractile dysfunction and has been implicated in the development of fatal RV arrhythmias.

The root cause of RV overloading and thus RV enlargement is pulmonary regurgitation (PR), which causes back flow of the blood into the RV. PR has been well studied qualitatively, and has been linked to many late problems such as RV arrhythmias, limited exercise tolerance , impaired RV function, and in some, sudden death [Therrien et al., 2002; Therrien et al., 2001; Rosenthal 1993].

However, there is a paucity of quantitative data characterizing PA flow in general, let alone in rTOF. Experimentally, Yoganathan et al., 1986 conducted some of the earliest *in-vitro* experimental studies on blood flows through PA using rigid cast models of human PA [Yoganathan et al., 1986]. Sung et al. extended the experimental study to pulsatile [Sung et al., 1990a; Sung et al., 1990b, c] flows through PA. To define these characteristics in a patient-specific manner encompassing geometric variations [Huang et al., 2009; Tang et al., 2007], computational modeling is necessary, thereby allowing calculation of pressure, flow [Shaik et al., 2007; Suo et al., 2008], and energy endpoints. Studies utilizing such techniques for PA flow characterization either utilized an idealized geometric model or a spatially-uniform velocity profile [Chern et al., 2008] as the boundary condition, failing to account for anatomic variations and flow reversals near the arterial walls as observed in *in-vitro* and MRI based *in-vivo* studies.

With the advent of phase contrast MRI [Fogel et al., 1994; Laffon et al., 2006;

Laffon et al., 2001a] it is possible to investigate the blood flow patterns in branch PA non-invasively. Cine phase contrast MRI makes it possible to obtain *in-vivo* velocity measurements in and out of a planar cross-section at any location in an artery, and has been employed to study three dimensional flow profiles in the PA of normal subjects [Morgan et al., 1998]. In addition, Womersley type velocity profiles [Womersley 1955] have been used in numerical computations of blood flows in other pathophysiologies [Taylor et al., 1998; Ryval et al., 2004] and is considered better approach for applying velocity boundary conditions as compared to a simplified profile such as spatially uniform or parabolic at any instant of time of a pulse cycle.

The aim of this study was to model branch PA blood flow in both normal and rTOF subjects using patient specific geometry, reconstructed from the individual MRI images, and use Womersley type velocity boundary conditions obtained from non-invasive cine phase contrast MRI flow measurements at the main PA (MPA) inlet and the left (LPA) and the right PA (RPA) outlets.

2 Methods

2.1 Study Population

Two age-, sex- and size-matched subjects, one normal (Age: 4 years, Sex: male, Wt.: 20.3 Kg, BSA: 0.78 m^2, Stroke volume: 52 ml) and the other rTOF (Age: 5 years, Sex: male, Wt.: 16.9 Kg, BSA: 0.72 m^2, Stroke volume: 56 ml) were selected. Data was retrospectively analyzed from records for each of the subjects who had undergone both clinical cine-phase-contrast magnetic resonance (CMR) imaging and cardiac catheterization within a span of 1 month at our center (Table 1). The Institutional Review Board of our center approved the study. The "normal" subject in our study had a normal RV loading along with a functioning pulmonary valve (PV; as confirmed by exam and echocardiography). The normal subject had relatively lower average LPA flow (1.85 ml/sec) compared to his RPA (46.6 ml/sec) and MPA flows (47.5 ml/sec) as obtained from phase contrast MRI measurements. The rTOF subject had been diagnosed of TOF and underwent clinical CMR at least 3 years after undergoing rTOF surgery in their infancy, including PV transannular patching, and had essentially a non-functional PV. The PV in the rTOF subject had been previously assessed by echocardiography and was found to be non-functional, with severe PV insufficiency but no stenosis. Neither of the subjects showed more than mild tricuspid regurgitation on echo.

Table 1: Patient demographics and clinical data.

	Age (years)	Height (m)	Weight (Kg)	BSA (m^2)	Heart rate (bpm)		MRI-Cath. Time Gap (Days)
					Catheter	MRI	
Normal: Normal RV & PV	4	1.11	20.3	0.78	85	79	19
rTOF: Abnormal RV & PV	5	1.07	16.9	0.72	102	100	2

2.2 Data Acquisition

Pulmonary Artery MRI Imaging. A stack of 3D MRI coronal images of the individual patient's chest that covered segments from the main, left and the right PA branch were acquired using a Siemens 3 Tesla MRI scanner (Fig. 1A). These set of MRI images were used to construct patient specific branch pulmonary artery (PA) geometry of the individual subjects. The image series consisted of a spatially aligned stack of coronal images of the chest. Typically, the image sets for each subject consisted of 36-48 images at uniformly spaced slice locations. Typical echo time for the image acquisition was of 1.08 sec and repetition time was 2.84 sec. The typical image resolutions was 1.17mm x 1.17mm to 1.33mm x 1.33mm. The slice thickness varied from 2.2mm to 5mm. All images were 256x256 pixels in size.

CMR Pulmonary Artery Flow Imaging. Pulmonary Artery Flow Imaging was performed using retrospective ECG-gating, through-plane velocity-encoded phase contrast (PC) technique [Fogel et al., 1994; Chatzimavroudis et al., 2001; Kitajima et al., 2008; Fogel et al., 1992; Fogel et al., 2006; Forder et al., 2003; Laffon et al., 2001b] on Siemens 3Tesla Trio Magnet (Siemens, Inc., Malvern, Germany) with an 8-channel cardiac coil equipment. Each subject underwent their CMR study via general endotracheal anesthesia with breath holding technique. Velocity encoding limits were adjusted as needed for minimal peak to avoid aliasing of phase signal. PC imaging was performed at the mid-point of the main and each of the branch pulmonary artery with 18-22 phases at each PA site: main, left and right PA. Data computed included peak velocity, area of flow and flow rate (antegrade and retrograde) at each PA site: MPA, LPA and RPA respectively.

Cardiac Catheterization. Subjects underwent cardiac catheterization solely for clinical indications using standard pediatric cardiac cateterization techniques while under general endotracheal anesthesia. Hemodynamic measurements were performed during the catheterization by advancement of a fluid-filled catheter (Cook

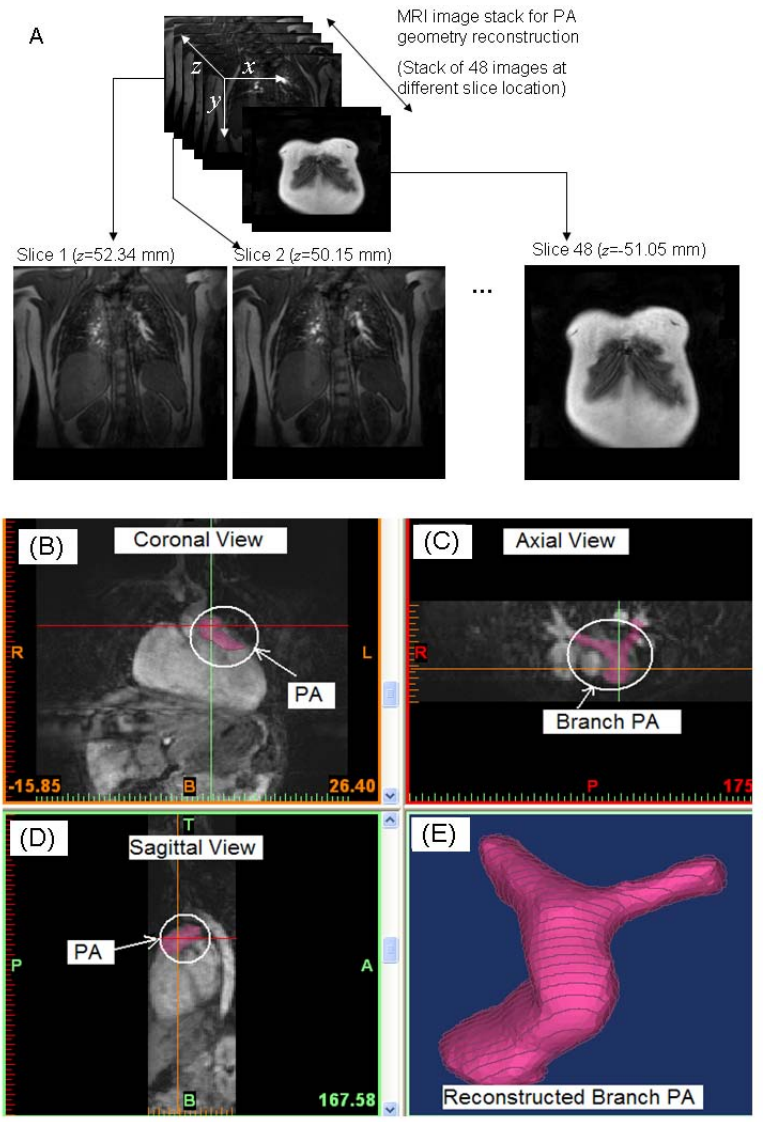

Figure 1: Geometry reconstruction from the patient specific MRI images: (A) Stack of 3D MRI images of subject's chest used for PA geometry reconstruction; (B), (C), (D) representing the coronal, axial and sagittal views respectively with PA identified by assigning masked by specifying grey scale value from the image. (E) The reconstructed branch PA geometry without the inlet and outlet cine-phase contrast velocity measurement planes. This geometry is exported as a file of STL triangles to create blood flow domain with inlet outlet surfaces which get defined by the velocity measurement planes.

Medical Inc., Bloomington, Indiana, USA) under fluoroscopic guidance into the RV and at least one of the following: main (MPA), left (LPA), or right (RPA) pulmonary artery. Pressure variation with time over the complete cardiac cycle at each site was recorded along with the ECG tracing on hard (paper) copy.

2.3 Data Analysis

Analysis of Pressure and Flow Data. PC images were analyzed via standard CMR flow assessment techniques using semi-automated computer software QFLOW (Medis Medical Imaging Systems, Inc., Leiden, Netherlands). Data computed included peak velocity, area of flow and flow rate (antegrade and retrograde) at each site, MPA, LPA and RPA, respectively. CMR and cardiac catheterization data were acquired at separate sessions. For our analyses, these data sets were adjusted to account for differences in heart rate between the sessions. This was performed digitally based on the resident electrocardiographic (ECG) signal present in both the data sets. This process required three steps for each subject. Initially, the hard-copy catheterization data (pressure versus time curves at MPA, and branch PA, and ECG versus time) were manually digitized between two consecutive ECG R-waves, from which the heart rate interval was determined. Next, the heart rate interval was measured from the digital CMR data (PA flow versus time), which by definition is recorded starting at the onset of the ECG R-wave. Finally, the CMR data was linearly scaled in the time domain to match the cardiac catheterization time period. All digital measurements and adjustments were performed via a customized MATLAB (MATLAB, Inc., Waltham, MA) program.

2.4 Blood Flow Model

PA Geometry Reconstruction. Patient specific PA geometry of each of the subjects was reconstructed from their individual contrast-enhanced 3D MRI images (Fig. 1A). The geometry reconstruction was done semi-automatically using MIMICS (Materialise, Inc., Leuven, Belgium). The geometry included the main PA, with its inlet located just distal to the pulmonary valve annular region, along with nearly equal lengths of the left and right pulmonary artery branches.

The stack of 3D MRI coronal images of the patient's chest were read into MIMICS image processing and geometrical reconstruction software. The software automatically computed spatial stack of axial and sagittal slices from the input coronal slices and showed the images on the three orthogonal views (coronal, axial and sagittal) as shown in the Fig. 1. The branch pulmonary artery was identified on any one of the views by visual inspection. The grey scale intensity values at the pulmonary artery location in the view were used to specify a threshold range for the software's region growing algorithm. The region growing algorithm in MIMICS automati-

cally created a volume of 3D voxels that match the specified intensity threshold range (Fig. 1B, 1C, 1D). Disjoint voxels that were not part of pulmonary artery volume were removed, resulting in one contiguous volume of PA geometry. This resulting volume still had surface roughness that were visually inspected and manually removed from the volume. Finally, a surface mesh of triangles was fitted to the volume of voxel to yield a smoothened geometry of the branch PA. The accuracy of the meshed surface was checked by projecting a sample of points on the PA boundary and by checking the projected distance to be within reasonable tolerance. This process results in boundary reconstruction of the blood flow zone without clearly defined inlet and outlet planes (Fig. 1E). The surface of this reconstruction was then exported as a stereolithographic (STL) file of surface triangles to define inlet and outlet surfaces and generate tetrahedral mesh in the blood flow domain (using GAMBIT, ANSYS, Inc., Canonsburg, PA).

Fluid Model. In this study, a pulsatile, non-Newtonian blood flow in the PA proximal and distal to the PA bifurcation was modeled, using rigid arterial wall assump-

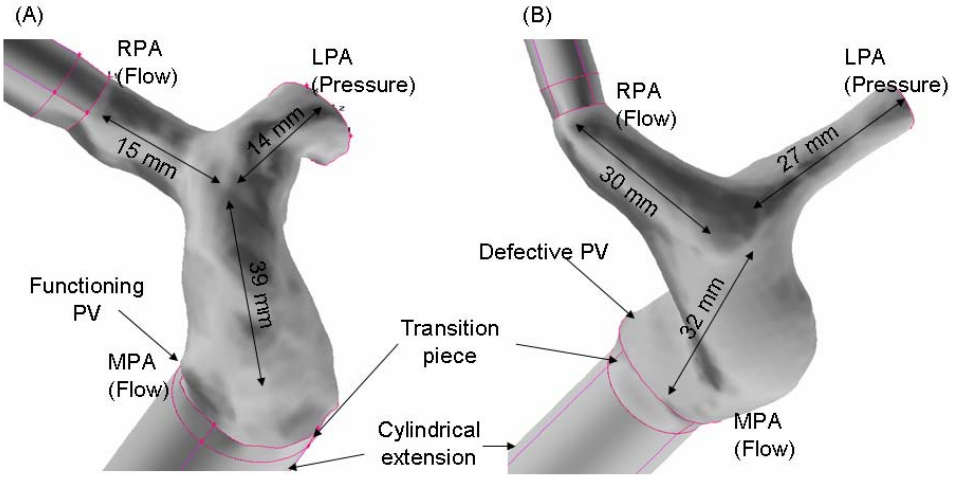

Figure 2: Geometrical model for blood flow computation. (A) Normal and (B) rTOF subject. The main PA domain is created from STL triangles. Inlet plane at MPA and outlet planes at LPA and RPA are created using plane locations and orientations from CMRI files. Cylindrical extensions are created to allow for flow development. Transition piece connects the cylindrical extension to the respective non-circular inlet or outlet. Since Womersley type velocity profile is used as velocity boundary conditions are applied, a much smaller extension is needed compared to other simplistic profiles such as uniform or parabolic.

tion. The geometry included the main PA, with its inlet located just distal to the pulmonary valve annular region, along with nearly equal lengths of the left and right PA branches. For our subjects, the typical main branch segment was of length 30-40 mm, and the left and the right branches were of lengths 15 mm to 25 mm beyond the bifurcation point (Fig.2). The blood flow computations were carried out using a finite volume method to numerically solve the coupled continuity and momentum equations. The flow was assumed incompressible and pulsatile, with non-Newtonian viscosity modelled using Carreau model [Banerjee et al., 2000]. Following standard tensorial notation, the continuity equation for an incompressible flow is given by,

$$u_{i,i} = 0 \tag{1}$$

and the momentum conservation equation for a non-Newtonian flow is given by,

$$\rho\left(\frac{\partial u_i}{\partial t} + u_j u_{i,j}\right) = -p_i + \left[\mu\left(u_{i,j} + u_{j,i}\right)\right]_j + \rho f \tag{2}$$

where, $\boldsymbol{p}$ is the static pressure and μ, the viscosity of the blood, which for a non-Newtonian fluid is defined by the ratio of shear stress to shear rate and is a tensor field.

Material Model. The blood was modelled as incompressible, shear thinning non-Newtonian fluid of density, ρ = 1.05 gm/cc. The blood viscosity was modelled using Carreau model [Banerjee et al., 2000] with shear rate ($\dot{\gamma}$) dependent viscosity μ given by,

$$\mu\left(\dot{\gamma}\right) = \mu_\infty + \left(\mu_0 - \mu_\infty\right)\left(1 + A\dot{\gamma}^2\right)^n \tag{3}$$

with the parameters, μ_∞= 0.345 poise, μ_0 = 0.56 poise, A= 10.975 sec^2, n = 0.3568, and the shear rate $\dot{\gamma}$ (in sec^{-1}) given by,

$$\dot{\gamma} = \sqrt{\frac{1}{2}\left[\sum_i \sum_j \dot{\gamma}_{ij}\dot{\gamma}_{ji}\right]} \tag{4}$$

Boundary Conditions. The blood flow calculations for both subjects were performed by applying pulsatile pressure boundary condition (BC) at the LPA outlet and spatially and time varying Womersley type velocity profiles at the boundary of the extended cylindrical MPA inlet and RPA outlet (please see mesh generation section). The digitized pressure measurements at the LPA was converted to a Fourier series, then synchronized with the flow-rate versus time curve as described

in the previous section. The Womersley type velocity profiles described in the next section were computed from the measured flow rate at the MPA and RPA locations. No slip condition was imposed on the arterial walls and the walls of the cylindrical extensions.

Womersley Velocity Profile from Flow Measurement. We present here the key steps to compute the velocity profiles at the MPA inlet and RPA outlet from the respective flow measurements. These computed profiles are applied as BC's at the inlet and outlets of the PA domain (for more details refer to [He et al., 1993]). Womersley's formulation [Womersley 1955] expresses the velocity profile at any cross-section for an unsteady, laminar flow of an incompressible fluid of density ρ and constant viscosity μ through a straight pipe of constant radius R, when time varying pressure gradient is available at any instant of time t. The velocity profile is expressed in terms of the coefficients of the complex Fourier series of the pressure gradient along the tube [Womersley 1955]. Flow rate can be obtained non-invasively and thus it is more useful to compute velocity profiles from flow measurements. The advantage of Womersley profile over simplistic velocity profiles such as spatially constant or parabolic type is that it is able to capture the flow reversal at walls and therefore, is a more realistic boundary condition for pulsatile flows than those simplistic profiles used in the prior studies. Here, such uniform or parabolic assumptions have been eliminated.

Using the measured flow-rate versus time data, the flow rate $Q(t)$ is approximated by a Fourier series with its coefficients computed from a set of $M-1$ uniformly sampled values of $Q(t)$. Thus, the period T of the pulse (cardiac period) is divided into M equal intervals of length Δt, with $\Delta t = T/M$, and the corresponding uniformly sampled time points t_s given by $t_s = s\Delta t$, $s = 0, 1, 2, \ldots, M-1$, with the corresponding sampled flow rate values as, $q_0 = Q(t_0)$, $q_1 = Q(t_1), \ldots, q_{M-1} = Q(t_{M-1})$ respectively. Using theses M-1 uniformly sampled values of flow rate versus time pulse, at the most $N = (M-2)/2$ harmonics of the Fourier series,

$$Q(t) = a_o + \sum_{k=1}^{N} \left\{ a_k \cos(k\frac{2\pi}{T}t) + b_k \sin(k\frac{2\pi}{T}t) \right\} \tag{5}$$

can be computed, and the corresponding Fourier series coefficients, a_o, a_1, ..., a_N and $b_1, \ldots, b_N$ are given by,

$$a_0 = \frac{1}{T}\int_0^T Q(t)dt = \frac{1}{M}\sum_{s=0}^{M-1} q_s \tag{6a}$$

$$a_k = \frac{2}{T}\int_0^T Q(t)\cos(k\omega_0 t)dt = \frac{2}{M}\sum_{s=0}^{M-1} q_s \cos(k\omega_0 t_s) \tag{6b}$$

$$b_k = \frac{2}{T}\int_0^T Q(t)\sin(k\omega_0 t)dt = \frac{2}{M}\sum_{s=0}^{M-1} q_s \sin(k\omega_0 t_s) \tag{6c}$$

The corresponding complex valued coefficients, Q_n's of the complex Fourier series,

$$Q(t) = \sum_{n=-N}^{N} Q_n e^{in\omega_0 t} \tag{7}$$

are computed using,

$$Q_n = \begin{cases} \frac{1}{2}(a_k + ib_k) & k = -n, \quad n < 0 \\ a_0 & n = 0 \\ \frac{1}{2}(a_k - ib_k) & k = n, \quad n > 0 \end{cases} \tag{8}$$

The equation for the Womersley velocity profile $u(r,t)$, at a radial location r from the face centroid and at a given instant of time t is given by [He et al., 1993],

$$u(r,t) = \frac{2Q_0}{\pi R^2}\left(1 - \frac{r^2}{R^2}\right) + \sum_{n=1}^{N} Real\left\{\frac{2Q_n}{\pi R^2}\left[\frac{1 - \frac{J_0(\alpha_n \frac{r}{R} i^{3/2})}{J_0(\alpha_n i^{3/2})}}{1 - \frac{2J_1(i^{3/2}\alpha_n)}{i^{3/2}\alpha J_0(i^{3/2}\alpha_n)}}\right] e^{inw_o t}\right\} \tag{9}$$

where, $Real(\cdot)$ is the real part of a complex number, J_0 and J_1 are the Bessel function of first kind of order 0 and 1 respectively [Relton 1949], and α_n is the non-dimensional Womersley number defined by,

$$\alpha_n = R\sqrt{\frac{2\pi n\rho}{T\mu}} \tag{10}$$

with T, R, ρ and μ being the period of the cardiac cycle, artery radius, blood density and viscosity, respectively and N representing the number of harmonics used to fit the experimental flow rate versus time data. Tables 2A and 2B provide the Fourier series coefficients for the MPA and the RPA flow rates for the first six harmonics along with the corresponding Womersley number for the normal and the rTOF subject respectively.

The formula for $u(r,t)$ given by Eq. 9 is implemented in our finite volume solver (FLUENT) using a user defined function as boundary condition.

3 Numerical Computation

Mesh Generation. The STL file of surface mesh of the branch PA wall (without the well defined inlet and outlet surfaces) was read into GAMBIT. Planes for the

Table 2A: Fourier coefficients and Womersley numbers (α_n) used to compute MPA and RPA flow profiles for the normal subject. Fourier coefficients expressed in polar form $2Q_n = M_n e^{i\phi_n}$. The fundamental frequency ω_0=8.49 rad/sec and the M_n values are in ml/sec.

Harmonics	Frequency (rad/sec)	MPA (Normal)			RPA (Normal)		
n	$\omega = n\omega_0$	α_n	M_n	ϕ_n	α_n	M_n	ϕ_n
0	0.0	-	47.42		-	46.38	-
1	8.49	0.1598	65.45	133° 51'	0.0871	49.52	127° 01'
2	16.98	0.2260	42.49	-90° 02'	0.1232	29.26	-112° 23'
3	25.47	0.2768	21.07	74° 14'	0.1509	9.50	95° 28'
4	33.96	0.3196	11.46	-89° 27'	0.1742	7.83	-66° 25'
5	42.45	0.3573	8.59	110° 10'	0.1948	4.20	122° 51'
6	50.94	0.3914	8.83	-53° 38'	0.2134	3.67	-51° 01'
7	59.43	0.4227	7.96	122° 10'	0.2305	2.50	132° 49'

Table 2B: Fourier coefficients and Womersley numbers (α_n) used to compute MPA and RPA flow profiles for the rTOF subject. Fourier coefficients expressed in polar form $2Q_n = M_n e^{i\phi_n}$. The fundamental frequency ω_0=10.70 rad/sec and the M_n values are in ml/sec.

Harmonics	Frequency (rad/sec)	MPA (Normal)			RPA (Normal)		
n	$\omega = n\omega_0$	α_n	M_n	ϕ_n	α_n	M_n	ϕ_n
0	0.0	-	41.84		-	19.63	-
1	10.70	0.1642	116.48	0	0.0848	38.72	-65° 10'
2	21.40	0.2322	40.17	-46° 44'	0.1199	13.89	127° 54'
3	32.11	0.2844	1.91	171° 03'	0.1468	4.68	-119° 22'
4	42.81	0.3284	7.02	-139° 24'	0.1695	1.51	129° 05'
5	53.51	0.3672	2.96	153° 24'	0.1896	1.06	135° 37'
6	64.22	0.4022	1.02	129° 04'	0.2076	0.67	-71° 31'
7	74.93	0.4345	1.18	-152° 53'	0.2243	0.44	-128° 24'

MPA inlet, and the LPA and RPA outlets, were created in GAMBIT by obtaining the respective plane locations and orientations from the phase-contrast images for velocity measurement at the MPA, LPA and RPA. Using the planes normal to the flow direction at the respective inlet and outlets, planar inlet and outlet surfaces were created in the volume. The region of the PA bounded by the inlet and outlet planes was meshed with linear tetrahedral elements of size 1 mm, resulting in

typically a range of 150K elements (Fig. 2). A finer mesh with elements in the range of 650K elements was used to check that the computed solution did not vary with mesh size. The non-circular inlet and outlet surface of the PA region were extruded to about 2-3 mm in the outward normal direction and also transitioned to a circular cross-section. The circular surface of the resulting transition piece was further extruded in the outward normal direction by 20 times the diameter to create cylindrical extensions (Fig. 2). Velocity boundary conditions were applied at the end of the cylindrical extensions.

Solution. The solution of the governing equations using above boundary conditions was performed in the finite volume solver FLUENT (ANSYS, Inc., Canonsburg, PA) using unsteady laminar flow model. The peak Reynolds number for our flow was in the laminar range. Thus an unsteady laminar flow model was used. Considering such flows, we do not rule out possible local shear layer instabilities and organized vortical cells at the locations of flow reversal. However, we will not categorize these as turbulent flow having random fluctuations in the PA.

The computations were performed for three cardiac cycles. Convergence of the numerical solution for each case was verified by performing mesh convergence study by reducing the mesh size from 1 mm to 0.5 mm and also by reducing the time steps from 0.001 sec to 0.0005 sec [Liu et al., 2004]. The flow rates and pressures from mesh convergence computations were verified to be between 1-5%. More specifically, the maximum difference in MPA pressure between results from computations with finer and the coarser mesh was found to be 3.4%.

With the above computational fluid dynamics (CFD) methodology, the velocity was computed at the LPA and pressures were computed at the RPA and MPA. The velocity field at LPA was used to compute LPA flow rate which was compared with the measured flow rate for validation. We also computed forward (Q_f) and reverse flow volume (Q_b), and regurgitant fraction (f) [Kang et al., 2003] at the LPA. The regurgitant fraction (f) is defined as the ratio of the reverse flow volume (Q_b) to the forward flow volume (Q_f) at any cross-section, and is expressed as a percentage. Likewise, area weighted average pressure at MPA and RPA were compared with the measured pressure data at those respective locations.

4 Results

MPA Regurgitant Fraction. The regurgitant fractions at the MPA for both the normal and rTOF subjects were calculated using the respective flow rate pulse (Fig. 3A and 3B) and were found to be 1.5% and 33.2% respectively; at the RPA, regurgitant fractions were 0% (normal subject) and 21.7% (rTOF), as expected. Such larger f values at MPA have been reported by others for rTOF patients [Kang et al.,

2003].

Table 3: Forward flow volume $Q_{f,}$, and back flow volume Q_b, per cardiac cycle for the normal and the rTOF subject computed from the measured flow rates at MPA and RPA. Regurgitant fraction (%) f = (Q_b/ $Q_{f,}$)100.

	Normal			rTOF		
	Q_f (ml)	Q_b (ml)	f (%)	Q_f (ml)	Q_b (ml)	f (%)
MPA	35.0	0.50	1.5	37.18	12.33	33.2
RPA	34.4	0.0	0.0	14.97	3.24	21.7

Flow Validation. The quantitative validation of our results from numerical computation with the measured data is presented in Fig. 5 and 6. Figure 5 shows the pulse of the computed and the measured flow rate at the LPA for both the normal and the rTOF subject. The results for Q_f, Q_b and the regurgitant fraction (f) are tabulated in Table 4 for both our normal and the rTOF subject.

The forward flow volume Q_f at the LPA per cardiac cycle for the normal subject from our numerical computation was 6.52 ml compared to 6.09 ml from the flow measurement (7% error). For the same subject, the reverse flow Q_b from our computation was 5.83 ml compared to 4.72 ml from measurements (23% difference). For the normal subject, the value of regurgitant fraction based on the numerical LPA flow was 89% compared to 77.5% from the measured flow curve (15.5% higher). High regurgitant fractions at LPA have been reported in earlier studies [Morgan et al., 1998; Kang et al., 2003]. The time averaged LPA flow rate for the normal subject, from the numerical LPA flow curve was 0.92 ml/sec, compared to 1.85 ml/sec for the experimental curve. Likewise for the same subject, the maximum and the minimum values of the LPA flow rate from our numerical computation were 50.5 ml/sec and -41.8 ml/sec, respectively, compared with 45.2 ml/sec and -22.5 ml/sec, respectively, from the measured flow rate curve.

Table 4: Validation of the numerical and measured result for LPA flow characteristics ($Q_{f,}$, Q_b and regurgitant fraction f) for the normal and the rTOF subject. Regurgitant fraction (%) f defined as (Q_b/ $Q_{f,}$)100.

	Normal			rTOF		
	Q_f (ml)	Q_b (ml)	f (%)	Q_f (ml)	Q_b (ml)	f (%)
Numerical	6.52	5.83	89.0	23.1	9.96	43.0
Measured	6.09	4.72	77.5	14.3	5.65	39.6
Error (%)	7.0	23.0	15.5	62.0	75.0	8.7

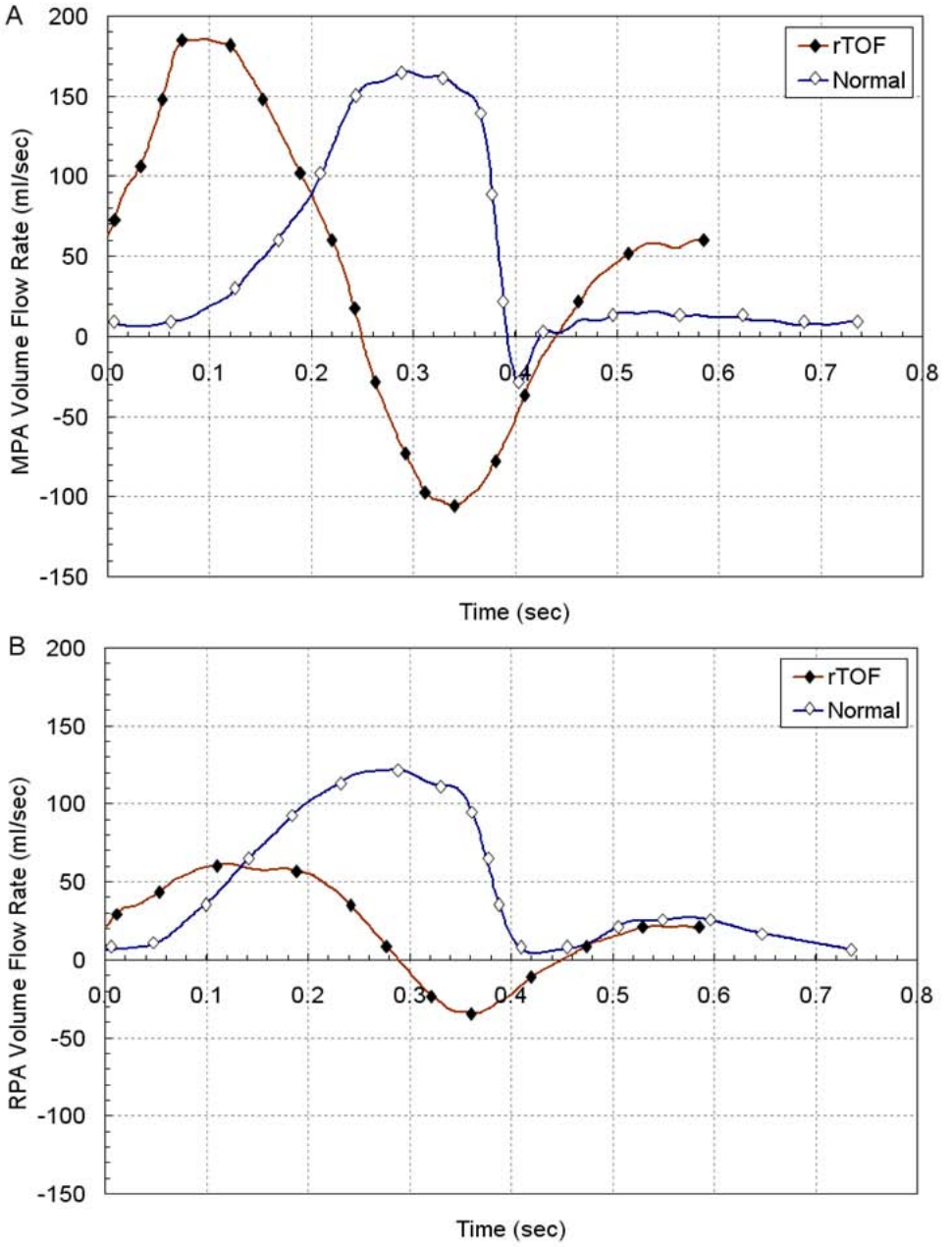

Figure 3: Measured flow rates pulse at A) MPA and B) RPA for the normal and the rTOF subject measured using cine-phase MR images. Womersley type velocity profiles are computed from these flow rates to be used as boundary conditions for the blood flow computation. The small back flow in the figure A at the MPA of the normal subject is expected.

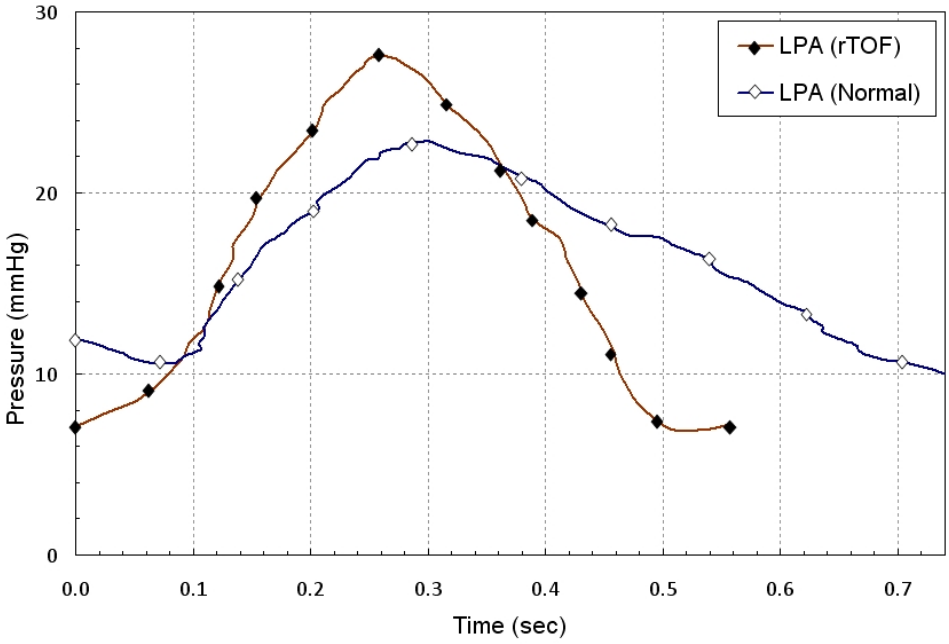

Figure 4: Pressure profile at the LPA, measured using fluid filled catheter for both the normal and the rTOF subject, and was applied at the LPA outlet as pressure boundary condition for blood flow computation.

Table 5: Validation of the numerical MPA and RPA pressure with measured data for the normal subject. The numbers represent time averaged pressure.

	MPA Pressure (mmHg)			RPA Pressure (mmHg)		
	Average	Min	Max	Average	Min	Max
Numerical	16.5	8.7	25.4	13.8	7.1	22.7
Measured	16.3	9.3	23.0	14.6	8.9	19.4
Error (%)	1.0	-6.0	10.0	-6.0	-20.0	17.0

For the rTOF subject, the forward flow Q_f at the LPA per cardiac cycle from the numerical computation was 23.1 ml compared to 14.3 ml from measurement (60% difference). The reverse flow volume Q_b at the LPA from computation was 9.96 ml compared to 5.65 ml from measurement, per cardiac cycle (75% difference). The regurgitant fraction in the LPA for the rTOF was 43% compared to 39% (experimental), an 8.7% difference. The time averaged LPA flow rate from the numerical curve was 22.4 ml/sec compared with the value of 14.6 ml/sec computed from the

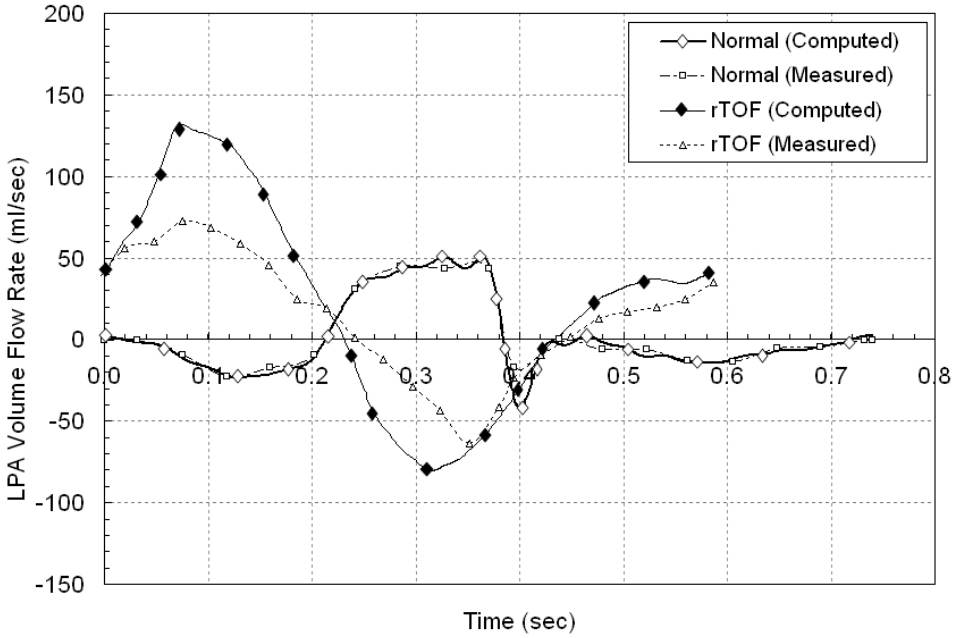

Figure 5: Validation of the numerical results. Validation of the computed flow rates at LPA with the measured flow rate at LPA for both the normal and the rTOF subject. The results from our numerical computation for the normal subject match very well with the measured flow rate at LPA whereas, the numerically computed flow rate at LPA of the rTOF subject shows some difference in values from the measured flow rate, although the trend is captured by our computation.

measured data. The peak flow rate from the numerical curve was 131.8 ml/sec, compared to 72.7 ml/sec from the measured data; and the minimum flow rate for the numerical and measured curves are, 80.3 ml/sec and 63 ml/sec respectively.

Pressure Validation. The results for MPA and RPA pressure variation with time for our normal subject are shown in Fig. 6A and 6B respectively. Figure 6A shows that the MPA pressure variation with time from our numerical computation follows the same trend as the measured MPA pressure. The time-averaged MPA pressure of 16.5 mmHg calculated from our numerical computation is in agreement with the time average value of 16.3 mmHg (1% difference) calculated from the measured data with (Fig. 6A). The peak MPA pressure from our numerical computation (25.4 mmHg) was found to be 10% higher than of the peak of the measured curve (23 mmHg). Likewise, the minimum value of the MPA pressure of 8.7 mmHg from our numerical calculation was found to be 6% lower than the minimum value of

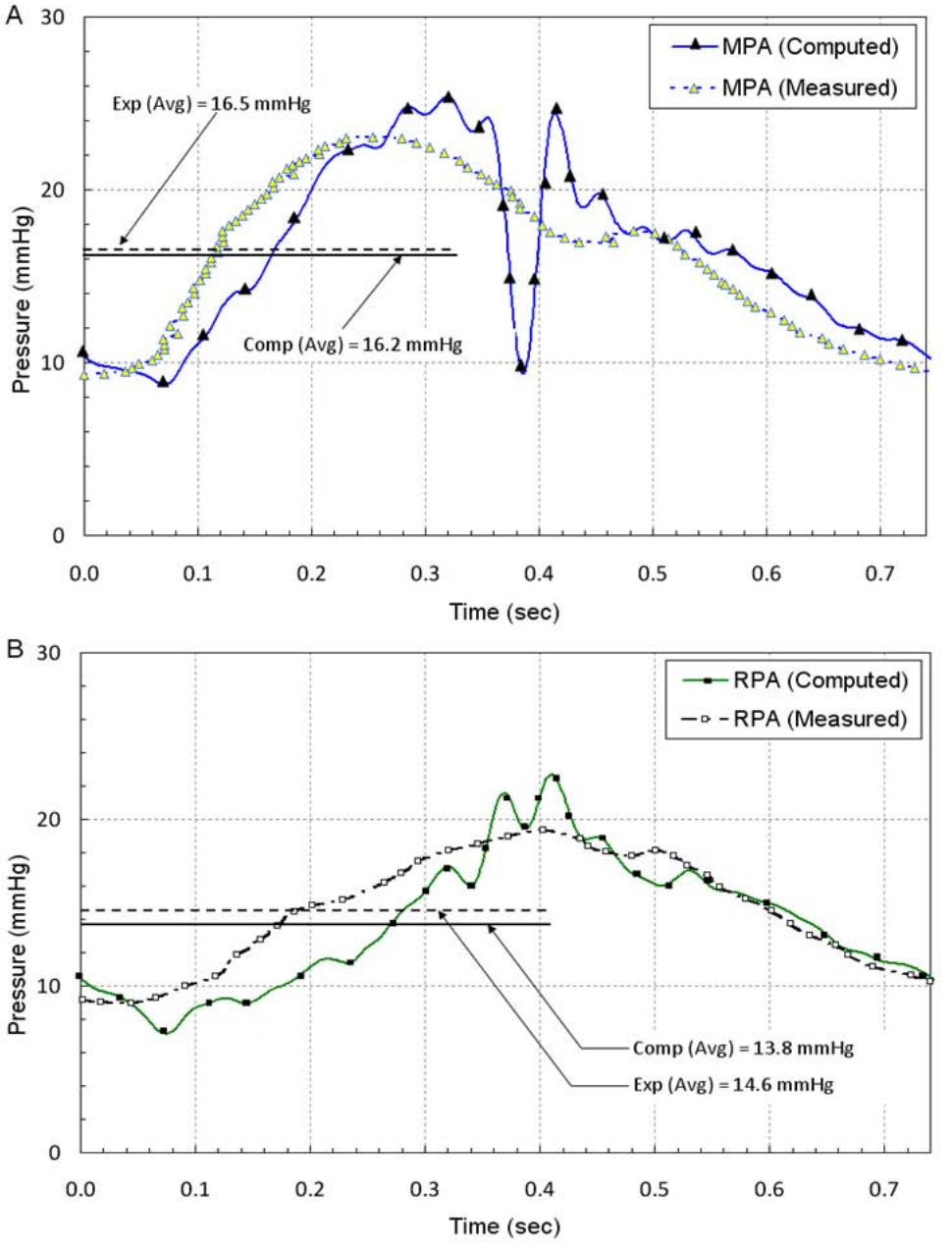

Figure 6: Validation of the computed pressures at (A) MPA and (B) RPA of our normal subject with the measured pressure at the respective locations. The average values for both computational (Comp) and measured (Exp) are depicted using horizontal lines. For our rTOF subject, no measured pressure data at the corresponding locations were available (since subjects were retrospectively selected for this pilot study and emphasize was placed on physiological similarity).

9.3 mmHg from the measured (Fig 6A). A sudden drop in MPA pressure value at around 0.38 sec was the result of sudden deceleration of flow at the point of closing of the PV for the normal subject. Although the measured pressure at MPA (Fig. 6A) for the normal subject also shows a slight drop at around 0.38 sec, the drop in value is not as pronounced. The numerical results for pressure are summarized in Table 5.

Figure 6B, RPA pressure versus time, also shows agreement between the numerical and the measured curves, in both, trend as well as time-averaged values. The time average values from the numerical RPA pressure curve is 13.8 mmHg (6% lower) compared with 14.6 mmHg from the measured one (Table 5). The peak value of the numerical RPA pressure curve (22.7 mmHg) was found to be 17% higher than that of the measured curve (19.4 mmHg). Similarly, the minimum value of the numerical RPA pressure curve of 7.1 mmHg was found to be 20% lower than the minimum value of 8.9 mmHg of the measured RPA pressure curve.

5 Discussion

This study validates the concept that numerical methodology coupled with CFD can be employed with clinically acquired CMR data to characterize intravascular hemodynamics in subjects with both normal and abnormal RV and PA pressure-flow physiology. Our geometry reconstruction from patient MRI data recreates the actual geometry closely, as opposed to artificial constructs that are often employed by extruding assumed geometrical shapes along a path approximated from arterial centerline.

Our measurements of flow rates at the MPA for our normal and rTOF subjects (Fig. 3) show that the MPA attains its peak flow rate rather rapidly for the rTOF subject compared to the normal one. This difference is likely due to the presence of the functioning PV in the normal subject.

The LPA regurgitant fraction for the normal subject (Table 4) is high for both the numerical and the measured value and is not unexpected [Morgan et al., 1998; Kang et al., 2003]. However, as expected the MPA regurgitant fraction is much smaller for the normal subject (by 95%) compared to the rTOF subject (Table 3). This is because of the functioning PV which prevents backward flow.

It can be seen from Table 4 that for the normal subject, our computation capture systolic behaviour of the LPA flow, with the LPA Q_f differing by only 7% between numerical and measured forward flow volume. In the diastolic phase, the LPA Q_b differs by 23% between the numerical and the measured LPA flow curves (Fig. 5). In this patient measured LPA flow was significantly lower than MPA and RPA flow. Thus, even though there is a significant agreement in LPA flow results between

numerical and measured flow values in the systolic phase of the cardiac cycle, the difference in the diastolic phase resulted in marginal difference in average flow rate (0.92 ml/sec from computation versus 1.85 ml/sec measured). It is known that CMR can be less accurate in registering reverse flow across the measurement plane hence further attention is needed for accurate flow measurement.

For the rTOF subject, Fig. 5 shows that our numerical results capture the time trend in the LPA flow rate. The regurgitant fraction (f) only shows a difference of 8.7%, showing that the flow rate trend is captured by our numerical calculation for the rTOF subject. The reason for difference between computed and measured LPA flow rate for the rTOF subject could be attributed to excessive regurgitation at MPA (MPA regurgitant fraction f=33.2% for the rTOF, versus 1.5% for the normal; Table 3). As mentioned above, that the CMR data can be less accurate in capturing reverse flow which could be a contributing factor in this case. Another potential contributor to this discrepancy is the likely to be the compliance effect PA wall (the functioning PV acts like a stiffener for the PA wall at the MPA), necessitating the need for a blood-PA wall interaction calculation and a more accurate velocity field estimation based on phase contrast MRI.

Our technique offer several methodological advances compared to prior studies. First, both the geometry and the velocity profiles are computed entirely from patient specific anatomic and phase contrast MRI data, a non-invasive methodology. More importantly, our use of Womersley type velocity boundary conditions are more realistic for transient flows because they are able to account for the flow reversal locally near the arterial walls, a phenomena noted in experimental *in-vitro* pulsatile flow studies in the branch PA [Yoganathan et al., 1986; Sung et al., 1990a; Sung et al., 1990b]. Assumed simplistic velocity profiles such as spatially uniform or parabolic profiles do not account for local flow variations. Although we have used long extensions in our computation, such long lengths may not be required because the Womersley profile represents a developed flow condition. With non-Newtonian fluid, as in our case, the Womersley profile will adjust to developed flow profile over much shorter length compared to a parabolic or uniform profile, thus requiring much shorter extensions.

Limitations. One limitation of this study is that the pressure (via catheterization) and flow/anatomic (via CMR) data were not acquired simultaneously, requiring the use of the ECG wave form to synchronize "offline" the pressure and the flow pulse. The difficulty in obtaining simultaneous pressure and flow/velocity data is well known but in our case we expect our synchronization of pressure and flow using ECG to be reasonable.

In addition, although the Wormesley velocity profile is an improvement as noted above, it does not precisely capture the velocity field realistically. Both phase con-

trast MRI measurements [Morgan et al., 1998], and *in-vitro* branch PA pulsatile flow studies [Sung et al., 1990b, c] report asymmetry in velocity field near PV, where as Womersley flow profile is axially symmetric. A direct use of phase contrast MR data may provide better results, as it will be able to account for asymmetry as well as flow reversal near the PA walls.

Finally, in this pilot study, since our patient sample was retrospectively selected, we are limited by the availability of the measured data for our subjects. For example for our rTOF subject, only the LPA pressure measurement was available and thus validation of the numerical results for MPA and RPA pressures with the respective pressures measurements was not possible.

6 Conclusion and Future Work

In this proof of concept study, we have demonstrated that CMR-based CFD methodology using patient-specific PA geometry and cine phase contrast MRI images of velocity fields at specific locations can be used to model realistic blood flow computations. Further research is currently underway to apply these techniques to a larger population of normal and abnormal subjects and obtain patient specific pressure, flow and energy based diagnostic endpoints to analyze PI and RV enlargement in rTOF patients.

References

1. d'Udekem, Y., Ovaert, C., Grandjean, F., Gerin, V., Cailteux, M., Shango-Lody, P., Vliers, A., Sluysmans, T., Robert, A., & Rubay, J. (2000) *Circulation* 102, III116-122.

2. Park, M. K. (1996) *Pediatric cardiology for practitioners* (Mosby, St. Louis).

3. Therrien, J., Marx, G. R., & Gatzoulis, M. A. (2002) *Cardiol Clin* 20, 395-404.

4. Therrien, J., Siu, S. C., Harris, L., Dore, A., Niwa, K., Janousek, J., Williams, W. G., Webb, G., & Gatzoulis, M. A. (2001) *Circulation* 103, 2489-2494.

5. Rosenthal, A. (1993) *N Engl J Med* 329, 655-656.

6. Yoganathan, A. P., Ball, J., Woo, Y. R., Philpot, E. F., Sung, H. W., Franch, R. H., & Sahn, D. J. (1986) *J Biomech* 19, 129-146.

7. Sung, H. W., Philpot, E. F., Nanda, N. C., & Yoganathan, A. P. (1990a) *J Biomech* 23, 563-578.

8. Sung, H. W. & Yoganathan, A. P. (1990b) *J Biomech Eng* 112, 88-92.

9. Sung, H. W. & Yoganathan, A. P. (1990c) *J Biomech* 23, 201-214.

10. Huang, X., Yang, C., Yuan, C., Liu, F., Canton, G., Zheng, J., Woodard, P. K., Sicard, G. A., & Tang, D. (2009) *Mol Cell Biomech* 6, 121-134.

11. Tang, D., Yang, C., Geva, T., & del Nido, P. J. (2007) *Mol Cell Biomech* 4, 159-176.

12. Shaik, E., Hoffmann, K. A., & Dietiker, J. F. (2007) *Mol Cell Biomech* 4, 41-53.

13. Suo, J., Oshinski, J. N., & Giddens, D. P. (2008) *Mol Cell Biomech* 5, 9-18.

14. Chern, M. J., Wu, M. T., & Wang, H. L. (2008) *J Biomech* 41, 3002-3009.

15. Fogel, M. A., Donofrio, M. T., Ramaciotti, C., Hubbard, A. M., & Weinberg, P. M. (1994) *Circulation* 90, 2927-2936.

16. Laffon, E., Latrabe, V., Jimenez, M., Ducassou, D., Laurent, F., & Marthan, R. (2006) *Eur Radiol* 16, 1442-1448.

17. Laffon, E., Laurent, F., Bernard, V., De Boucaud, L., Ducassou, D., & Marthan, R. (2001a) *J Appl Physiol* 90, 2197-2202.

18. Morgan, V. L., Roselli, R. J., & Lorenz, C. H. (1998) *Ann Biomed Eng* 26, 557-566.

19. Womersley, J. R. (1955) *J Physiol* 127, 553-563.

20. Taylor, C. A., Hughes, T. J., & Zarins, C. K. (1998) *Ann Biomed Eng* 26, 975-987.

21. Ryval, J., Straatman, A. G., & Steinman, D. A. (2004) *J Biomech Eng* 126, 625-635.

22. Chatzimavroudis, G. P., Oshinski, J. N., Franch, R. H., Walker, P. G., Yoganathan, A. P., & Pettigrew, R. I. (2001) *J Cardiovasc Magn Reson* 3, 11-19.

23. Kitajima, H. D., Sundareswaran, K. S., Teisseyre, T. Z., Astary, G. W., Parks, W. J., Skrinjar, O., Oshinski, J. N., & Yoganathan, A. P. (2008) *J Biomech Eng* 130, 041004.

24. Fogel, M. A. & Chin, A. J. (1992) *J Am Coll Cardiol* 20, 181-190.

25. Fogel, M. A., Weinberg, P. M., Harris, M., & Rhodes, L. (2006) *Am J Cardiol* 97, 1232-1237.

26. Forder, J. R. & Pohost, G. M. (2003) *J Clin Invest* 111, 1630-1639.

27. Laffon, E., Bernard, V., Montaudon, M., Marthan, R., Barat, J. L., & Laurent, F. (2001b) *J Appl Physiol* 90, 469-474.

28. Banerjee, R. K., Back, L. H., Back, M. R., & Cho, Y. I. (2000) *J Biomech Eng* 122, 310-320.

29. He, X., Ku, D. N., & Moore, J. E., Jr. (1993) *Ann Biomed Eng* 21, 45-49.

30. Relton, F. E. (1949) *Applied Bessel functions* (Blackie, London,).

31. Liu, Y., Pekkan, K., Jones, S. C., & Yoganathan, A. P. (2004) *J Biomech Eng* 126, 594-603.

32. Kang, I. S., Redington, A. N., Benson, L. N., Macgowan, C., Valsangiacomo, E. R., Roman, K., Kellenberger, C. J., & Yoo, S. J. (2003) *Circulation* 107, 2938-2943.